Chapter 8
Atomic and Electronic Structure of Silicene on Ag: A Theoretical Perspective

Seymur Cahangirov and Angel Rubio

The isolation of graphene sheets from its parent crystal graphites has given the kick to experimental research on its prototypical 2D elemental cousin, silicene [1]. Unlike graphene, silicene lacks a layered parent material from which it could be derived by exfoliation. Hence, the efforts of making the silicene dream a reality were focused on epitaxial growth of silicene on substrates. The first synthesis of epitaxial silicene on silver (111) [27, 46] and zirconium diboride templates [16] and next on an iridium (111) surface [31], has boosted research on other elemental group IV graphene-like materials, namely, germanene and stanene [30, 48]. The boom is motivated by several new possibilities envisaged for future electronics, typically because of the anticipated very high mobilities for silicene and germanene [49], as well as potential optical applications [30]. It is also fuelled by their predicted robust 2D topological insulator characters [14, 28] and potential high temperature superconductor character [5, 50]. One of the most promising candidates as a substrate is Ag because from the studies of the reverse system, where Ag atoms were deposited on silicon substrate, it was known that Ag and silicon make sharp interfaces without making silicide compounds

S. Cahangirov (✉)
UNAM - National Nanotechnology Research Center, Bilkent University,
06800 Ankara, Turkey
URL: http://unam.bilkent.edu.tr/seymur

A. Rubio
Max Planck Institute for the Structure and Dynamics of Matter
and Center for Free-Electron Laser Science, Luruper Chaussee 149,
22761 Hamburg, Germany
URL: http://www.mpsd.mpg.de/en/research/theo

A. Rubio
Nano-Bio Spectroscopy Group and ETSF, Dpto. Fisica de Materiales,
Universidad del País Vasco, CFM CSIC-UPV/EHU-MPC and DIPC,
20018 San Sebastián, Spain
URL: http://nano-bio.ehu.es/

P. Vogt and G. Le Lay (eds.), *Silicene*, NanoScience and Technology,
https://doi.org/10.1007/978-3-319-99964-7_8

[24]. Indeed, studies on synthesiz and characterization of silicene is mainly focused on using Ag(111) as substrates and hence we think it is important to understand this particular system. In this Chapter, we present a theoretical perspective on the studies investigating the atomic and electronic structure of silicene on Ag substrates.

8.1 The 3 × 3 Reconstruction

Silicene was synthesized for the first time on Ag(111) substrates [46]. Their STM measurements revealed the "flower pattern" originating from protruding atoms of 3×3 reconstructed silicene matching the 4×4 supercell of the Ag(111) surface as shown in Fig. 8.1. This structure was also confirmed by DFT calculations where the geometry optimization starting from unreconstructed 3×3 supercell of silicene on top of 4×4 supercell of Ag(111) slabs resulted in the reconstructed silicene that reproduced the STM image observed in experiments. Note that, while bond lengths vary from 2.34 to 2.39 Å, the angle between the bonds spans a wide range starting from 108°, which is less than the ideal sp^3 bond angle, up to 120°, which is the ideal bond angle of sp^2 hybridization. Each of the three protrusions seen in STM image make a group of Si atoms that belong to the same silicene sublattice. However, there are two such groups in every 3×3 unitcell that belong to the different sublattices of silicene. This becomes evident when H is deposited on 3×3 silicene which results in a highly asymmetric STM image due to the fact that H atoms prefer to bind only to one of the two sublattices. The atomic structure of 3×3 phase of silicene was also confirmed by reflection high energy positron diffraction (RHEPD) as well as low energy electron diffraction (LEED) experiments [17, 23].

The archetype single layer silicene, which is the 3×3 phase having a unique orientation, results from a delicate balance between the impinging Si flux (yielding, typically, completion in about 30 minutes), the surface diffusion of the deposited Si atoms on the bare and silicene covered areas and the competing in-diffusion toward the sub-surface. The growth is driven by these kinetic processes, which, actually, gives a very narrow substrate temperature window of about 200–220 °C [27, 46]. Here silicene forms a highly ordered structure, which can cover 95% of the crystal surface [17], because of the exact correspondence between 3 silicene basis vectors and 4 nearest neighbor Ag–Ag distances. The "flower pattern" observed both in STM and non-contact AFM imaging results from the puckered Si atoms sitting nearly on top of Ag atoms, giving a total corrugation of ∼0.07 nm in the silicene sheet [36, 46].

Already from ∼250 °C a new 2D phase of silicene develops, co-existing with domains of the $3 \times 3/4 \times 4$ phase. Since control of the substrate temperature is not easy in this temperature regime where most pyrometers are inoperative and where thermocouples, depending on their locations, generally give improper values, in many cases, mixed $3 \times 3/4 \times 4$ and $\sqrt{7} \times \sqrt{7}/\sqrt{13} \times \sqrt{13}$ domains are simultaneously observed [27]. In the latter case, four rotated domains, imposed by symmetry are present, since the $\sqrt{7} \times \sqrt{7}$ silicene domains are rotated by $\pm 19.1°$ with respect

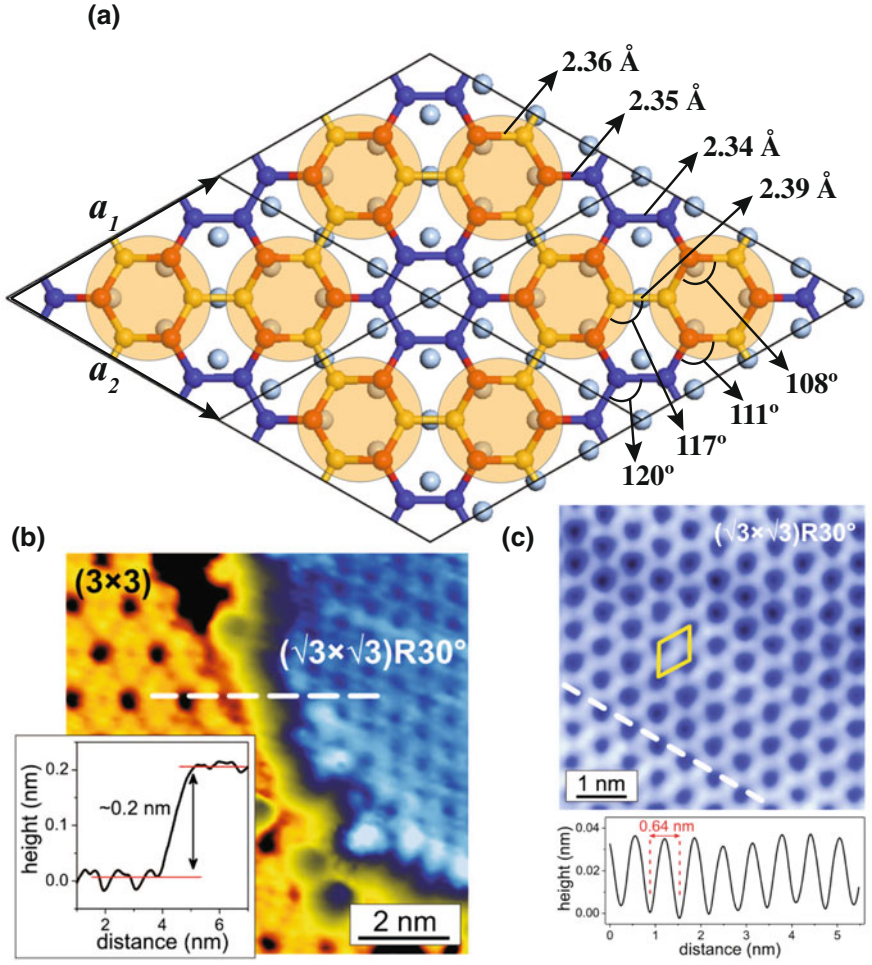

Fig. 8.1 **a** Top view of 3 × 3 silicene matched with a 4 × 4 Ag(111) surface supercell. Only the topmost atomic layer of Ag(111) is shown and represented by light blue balls. Red, yellow and blue balls represent Si atoms that are positioned near the top, hollow and the bridge sites of the Ag(111) surface. Red Si atoms that are positioned on top of Ag atoms protrude up. Yellow Si atoms are mainly interacting with the Ag atoms that sit under the bonds connecting them. When the STM resolution is not high enough, the three protruding red Si atoms are seen as a single dot represented by transparent orange circles drawn around them. These circles form large hexagons that have 3 × 3 periodicity. **b** STM image and line profile scanning from 3 × 3 to $\sqrt{3} \times \sqrt{3}$ silicene on Ag(111). **c** STM image and line profile of $\sqrt{3} \times \sqrt{3}$ silicene on Ag(111). Adapted from [45]

to each of the two $\sqrt{13} \times \sqrt{13}$ Ag super cells, which are themselves rotated by $\pm 13.9°$ with respect to the main [-110] and alike directions of the Ag(111) surface. These domains are buckled, differently from the 3 × 3/4 × 4 case and are accordingly slightly expanded, while remaining commensurate, to accommodate a 4% reduction

in Si coverage ratio (from $\theta_{Si} = 1.125$ for the $3 \times 3/4 \times 4$ phase to $\theta_{Si} = 1.077$ for this new one), signaling a self-healing process of the silicene mesh, while some of its atoms have disappeared below the surface. These four domains have been imaged simultaneously on the same STM topograph [36]. Details of these structures are discussed in Chap. 7.

8.2 The Nature of the Linear Bands

There is no doubt that the linear bands are one of the most intriguing features of silicene (see Chap. 2). Indeed, angle resolved photoemission spectroscopy (ARPES) measurements of the 3×3 silicene phase revealed a linear band starting 0.3 eV below the Fermi level and extending all the way down to -3 eV with a slope of $\sim 1.3 \times 10^6$ m/s [46]. This linear band was not detected when silicene was absent. However the extension and slope of the linear band was too high to be attributed solely to silicene. On the other hand, scanning tunneling spectroscopy (STS) measurement performed under high magnetic field applied in perpendicular direction to the 3×3 silicene on Ag substrate have shown that the peaks corresponding to the Landau levels corresponding to the presence of the Dirac fermions were absent while they were present in the highly oriented pyrolitic graphite samples [26]. This experimental result was supported by DFT calculations to conclude that Dirac fermions of ideal silicene were destroyed due to the symmetry breaking and hybridization with the Ag substrate. These results created a debate on the origin of the linear bands of silicene on silver.

The 3×3 reconstruction of silicene forms due to the interaction with the Ag substrate and breakes the symmetry needed to preserve the linearly crossing bands at the Fermi level. This is clearly seen in the band structure of the 3×3 reconstructed silicene isolated from the substrate presented in Fig. 8.2a. Here the band structure of the 3×3 reconstructed silicene is unfolded into the Brillouin zone of the ideal 1×1 silicene. Upon reconstruction, the linearly crossing bands are destroyed and instead there is a 0.3 eV gap at the K point. To interpret the ARPES experiments mentioned above, Cahangirov et al. calculated the electronic structure of 3×3 silicene placed on top of 11 layers of 4×4 Ag substrate [2]. Figure 8.2c shows the detailed band structure of the silicene/Ag system in the window where the experiments were performed (see Fig. 8.2b). The blue curve corresponds to the bulk Ag sp-band that should not be detected by ARPES which is sensitive to the surface states. Figure 8.2d and e show the states that have significant contribution from surface Ag states when silicene is absent and present, respectively. Here one can choose the threshold in such a way that the linear band disappears when silicene is absent and appears when it is present thereby mimicking the situation observed in ARPES experiments. This analysis suggests that the linear bands are caused by hybridization between silicene and Ag. The perpendicular momentum dependence of the electronic states was calculated by a k-projection technique and was used to calculate the contribution of silicene and Ag to the surface band created by hybridization [8]. This study provided further quan-

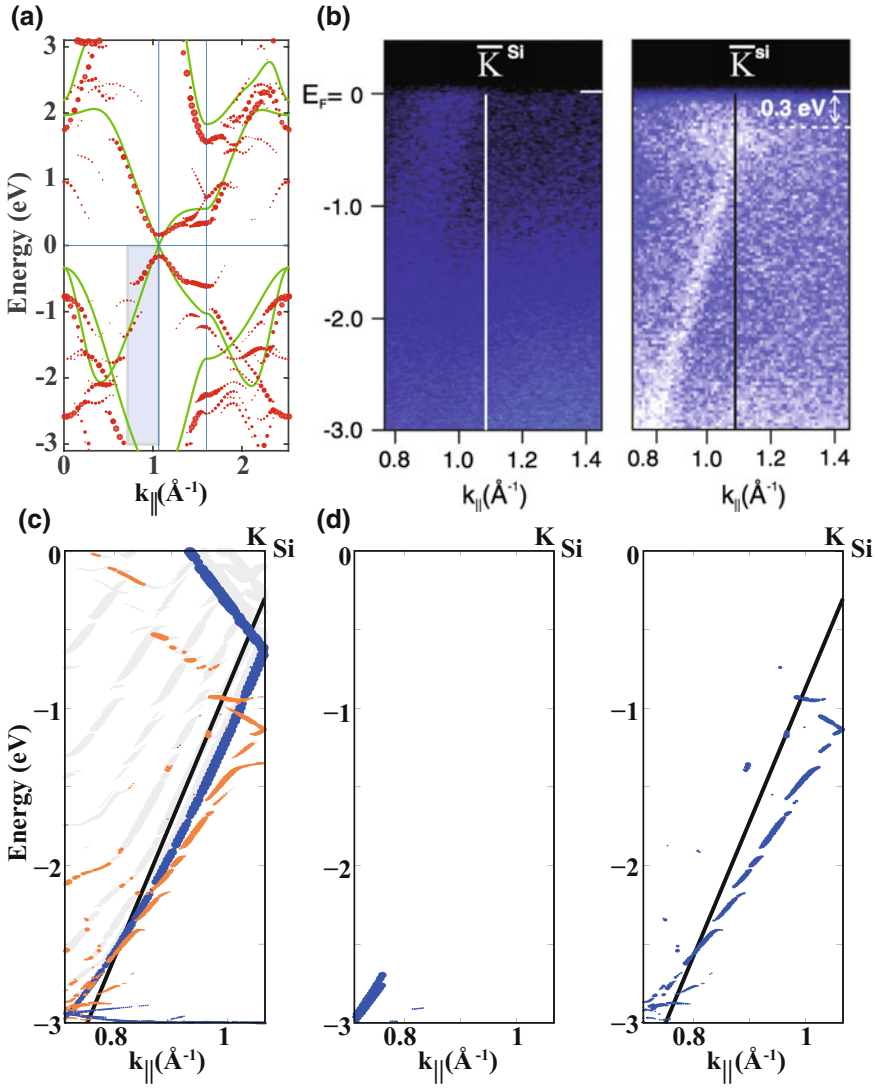

Fig. 8.2 **a** Band structure of reconstructed 3 × 3 silicene (red dots) in the absence of Ag substrate unfolded to 1 × 1 Brillouin zone of silicene. The dots radii correspond to the weight of the unfolded state. The band structure of ideally buckled silicene is shown by green lines. **b** ARPES data around the K point of 1 × 1 silicene in the absence (left panel) and presence (right panel) of silicene on Ag(111) substrate (adapted from [46]). **c** Band structure of 3 × 3 silicene a 4 × 4 Ag(111) 11 layer slab in the experimentally relevant range shown by the shaded region in (**a**). The states contributed by 3 Ag layers in the middle of the slab represent the bulk Ag states and are shown by blue lines. Orange lines are contributed by silicene and 3 Ag layers underneath. The black line represents the experimentally observed linear band. **d** States contributed by 3 Ag layers underneath silicene in the absence (left panel) and presence (right panel) of silicene. Adapted from [2]

titative agreement with experiments while confirming the hybridized nature of the experimentally observed linear bands. The surface band created by the hybridization between silicene and Ag was detected and distinguished from the faintly visible Ag *sp*-bands in the ARPES measurements [43]. There are many other investigations that have reached to conclusion that the linear bands are due to hybridization between silicene and Ag [18, 47].

The search for Dirac cones is not limited to the silicene on Ag substrates. ARPES measurements performed on calcium disilicide ($CaSi_2$) revealed a massless Dirac cone located at 2 eV below the Fermi level [32]. $CaSi_2$ can be considered as buckled silicene sandwiched between the planar atomic planes of Ca. The energy shift in the electronic states of silicene is due to significant charge transfer between Si and Ca atoms. First-principles calculations of the $CaSi_2$ structure revealed that there is, in fact, also a momentum shift in the Dirac cone away from the highly symmetric K point [13]. This is due to the symmetry breaking between the sublattice atoms of silicene and consequent asymmetric interlayer hopping. The shift in the momentum space is also accompanied with a small energy gap opening between the linearly crossing bands.

The Ag substrate plays a crucial role in growth of silicene, as seen from the previous section. This wouldn't be possible if the interaction between silicene and Ag was too weak. A first-principles study of the electronic charge density between silicene and the Ag(111) substrate has concluded that bonds between Si and Ag atoms don't have covalent character [41]. However, hybridization with Ag seems to interfere with the delicate electronic structure of silicene, as mentioned above. To avoid this, one has to develop techniques to transfer silicene to less interacting and insulating substrates. Tao et al. have taken an important step in this direction [42]. They first grew silicene on Ag and encapsulated it with alumina. Then they flipped the system upside down and etched Ag on silicene, just leaving two Ag pads that they used as metal contacts. In this way they have demonstrated that silicene can operate as an ambipolar field-effect transistor at room temperature.

8.3 The $\sqrt{3} \times \sqrt{3}$ Reconstruction

Another phase of silicene that is frequently observed to grow on Ag(111) substrate has a $\sqrt{3} \times \sqrt{3}$ reconstruction with respect to silicene unitcell. Unlike the other phases mentioned above, the $\sqrt{3} \times \sqrt{3}$ reconstructed phase of silicene is not matched by any lattice vector of the Ag(111) substrate [7, 15, 45]. The $\sqrt{3} \times \sqrt{3}$ reconstructed silicene was first reported by Feng et al. They measured the lattice constant to be 0.64 nm which is ~5% less compared to ideal silicene while the STM image was composed of bright triangular spots arranged in a $\sqrt{3} \times \sqrt{3}$ honeycomb lattice (see Fig. 8.1). They have also shown that the same STM image persists in the second layer which hinted that the $\sqrt{3} \times \sqrt{3}$ structure was intrinsic and not formed due to the matching with Ag substrate. Later the $\sqrt{3} \times \sqrt{3}$ reconstruction was also observed in multilayer silicene grown on Ag(111) substrates [45]. The distance between con-

secutive layers was measured to be around 3.0–3.1 Å. The STM images presented in Fig. 8.1 shows that the distance between neighboring 3×3 and $\sqrt{3} \times \sqrt{3}$ silicene is only 2 Å.

Several models were proposed to describe the origin and the atomic structure of the $\sqrt{3} \times \sqrt{3}$ reconstruction. One of them proposes that if monolayer silicene is squeezed enough, then the $\sqrt{3} \times \sqrt{3}$ honeycomb reconstruction becomes energetically more favorable than the ideal 1×1 buckling [7]. However, this happens if the lattice constant is squeezed down to ~6.3 Å and also there is no physical reason for the system to remain in this high energy state. Another model is based on the well studied Si(111)-Ag$\sqrt{3} \times \sqrt{3}$ system [12, 39]. This model also produces a $\sqrt{3} \times \sqrt{3}$ honeycomb pattern in STM measurements (see Fig. 8.6). In this case the bright spots are originating from Ag atoms on top of Si(111). However, it is not clear how the 3×3 structure is transformed into $\sqrt{3} \times \sqrt{3}$ structure with Ag atoms on top and also why the lattice is compressed. Yet another model suggests that the $\sqrt{3} \times \sqrt{3}$ honeycomb STM image is a result of the atomic scale flip-flop motion at the surface of bilayer Si(111) structure formed on top of the 3×3 structure [19]. Here the authors suggest that there are three possible configurations and the system is alternating between two of them. Since each state produces a trigonal STM pattern, the combination of two of them should produce the expected honeycomb pattern. However, there is no clear reason why the system should choose to alternate only between two states. Furthermore, this model does not explain the 5% lattice contraction observed in experiments [7, 15, 45].

The subsequent growth of $\sqrt{3} \times \sqrt{3}$ reconstructed silicene after formation of 3×3 silicene was studied by DFT calculations [4]. Here we summarize results of that study. As Si atoms are deposited on Ag(111) surface they search for the optimum structure that minimizes the energy. In the absence of the Ag substrate this optimum structure is the cubic diamond structure that has a cohesive energy of 4.598 eV/atom according to DFT calculations. However, in the presence of the Ag substrate a monolayer of silicene that has primarily 3×3 reconstruction is formed. Here, the 3×3 supercell of silicene is matched with the 4×4 supercell of the Ag(111) surface, as shown in the Fig. 8.1a. If we remove the Ag substrate and freeze the Si atoms of the 3×3 reconstructed silicene to calculate its cohesive energy, it turns out to be 3.850 eV/atom, which is 108 meV lower than the buckled freestanding silicene. In fact, if we start from the freestanding 3×3 reconstructed silicene and relax the structure, it goes to the buckled structure, meaning that it is not even a local energy minimum in the absence of the Ag substrate. However, the cohesive energy of 3×3 structure surpasses that of the cubic diamond structure when it is placed on the Ag(111) surface. This strong interaction between silicene and the Ag substrate explains the growth of monolayer silicene instead of clustering of Si atoms into bulk structures.

The model proposed by Cahangirov et al. to explain the growth of the $\sqrt{3} \times \sqrt{3}$ structure is based on the so called dumbbell structures. This peculiar structure emerges when a Si adatom is adsorbed on already formed silicene. As seen in Fig. 8.3, the Si adatom first attaches to dangling bonds of silicene and then forms bridge bonds with two-second neighbor Si atoms of silicene thereby increasing the coordination

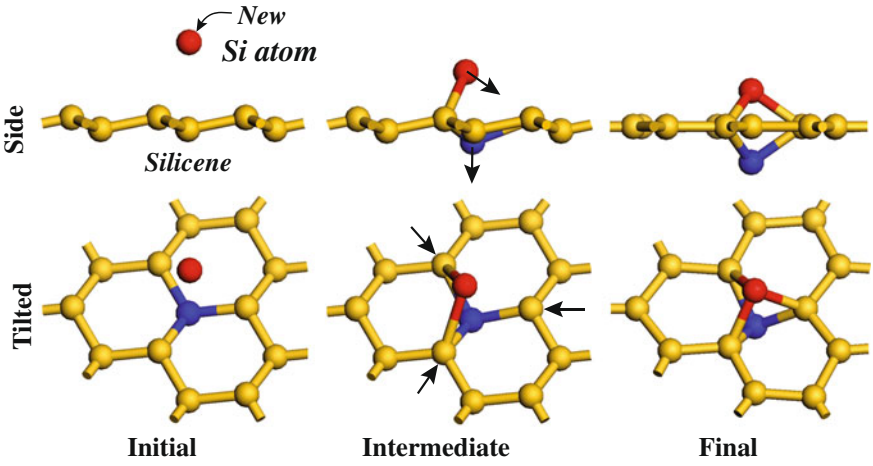

Fig. 8.3 Formation of the dumbbell building block units starting from freestanding silicene

number of these Si atoms from three to four. In search for tetrahedral orientation, these four bonds then force the atoms to move towards the directions shown in the middle panel of Fig. 8.3. As a result, the new Si adatom sits 1.38 Å above the top site of silicene while at the same time pushing down the Si atom just below it by the same amount. These two atoms are connected to other Si atoms by three bonds that are almost perpendicular to each other. The resulting geometry is called the dumbbell structure [4, 22, 34]. The dumbbell formation is an exothermic process and occurs spontaneously without need to overcome any kind of barrier. In the case of a C atom adsorbed on graphene, the dumbbell structure does not form because it is energetically less favorable compared to the configuration in which the C adatom is attached to the bridge site of graphene [35].

Calculations show that when a single dumbbell unit is placed in an $n \times n$ unit cell the cohesive energy per Si atom is maximized when $n = \sqrt{3}$ and decreases monotonically for $n \geq 2$ [4]. We refer to the structure having a single dumbbell unit in the $\sqrt{3} \times \sqrt{3}$ unit cell as trigonal dumbbell silicene (TDS) due to the trigonal lattice formed by dumbbell atoms, as shown in Fig. 8.4a [4, 22]. As seen in Table 8.1, TDS is energetically more favorable than freestanding silicene [22, 34]. Interestingly, the cohesive energy per Si atom is further increased when another dumbbell unit is created in the $\sqrt{3} \times \sqrt{3}$ unit cell of TDS. We refer to this new structure as honeycomb dumbbell silicene (HDS) due to the honeycomb structure formed by two dumbbell units in the $\sqrt{3} \times \sqrt{3}$ unit cell (see Fig. 8.4b).

The atomic structure of HDS is crucial to understand the $\sqrt{3} \times \sqrt{3}$ reconstruction that emerges when silicene is epitaxially grown on Ag(111) substrates since it is in excellent agreement with contracted lattice constant and STM image measured in experiments [4, 7, 15, 45]. Adding another dumbbell unit in the $\sqrt{3} \times \sqrt{3}$ unit cell of HDS results in a 1×1 structure composed of dumbbell atoms connected by sixfold

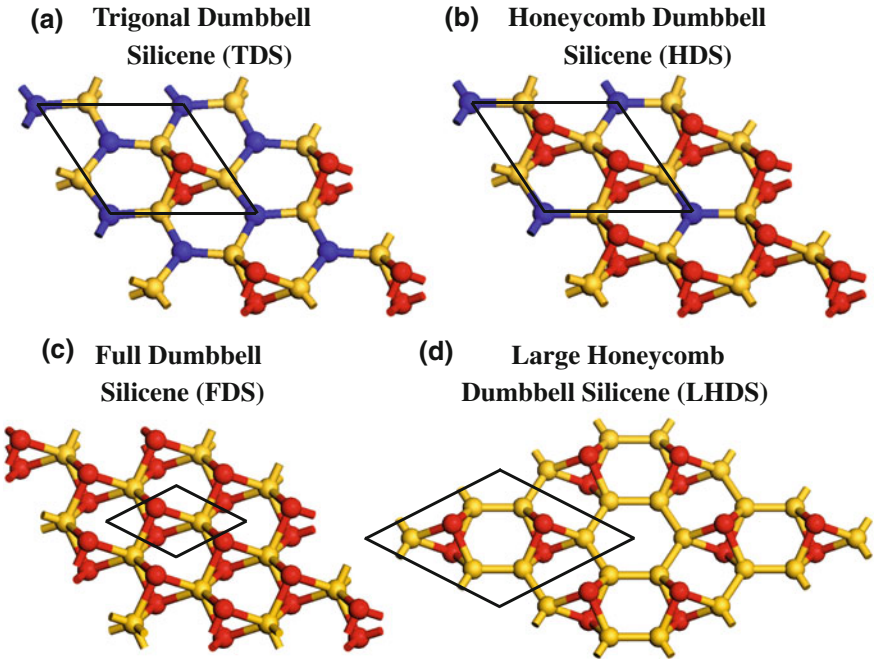

Fig. 8.4 Atomic structure of **a** $\sqrt{3} \times \sqrt{3}$ trigonal dumbbell silicene (TDS), **b** $\sqrt{3} \times \sqrt{3}$ honeycomb dumbbell silicene (HDS), **c** 1×1 full dumbbell silicene (FDS) and **d** 2×2 large honeycomb dumbbell silicene (LHDS). The unit cells are delineated by solid black lines. Atoms having different environment are represented by balls having different colors

Table 8.1 Cohesive energy and $\sqrt{3} \times \sqrt{3}$ lattice constant of buckled silicene compared with that of dumbbell structures

	Silicene	TDS	LHDS	HDS	FDS
Cohesive energy (eV/atom)	3.958	4.013	4.161	4.018	3.973
$\sqrt{3} \times \sqrt{3}$ lattice constant (Å)	6.69	6.52	6.43	6.38	6.23

coordinated Si atoms (see Fig. 8.4c). The cohesive energy of this structure, that we refer to as full dumbbell silicene (FDS), is less than that of TDS and HDS.

We should emphasize that it is the interplay between two competing effects that makes HDS the most favorable $\sqrt{3} \times \sqrt{3}$ structure. While formation of new dumbbells and thus new bonds increases the cohesive energy, the increase in the coordination number beyond four decreases it. As seen in Fig. 8.4, the coordination number of yellow atoms in the TDS structure is four while in HDS it is five. Apparently, the formation of a new dumbbell and hence new bonds compensates the energy required

Table 8.2 Cohesive energies per Si atom and per unit area are given for the 3×3 reconstructed silicene, TDS, LHDS, and HDS structures on the Ag(111) surface

	3×3	TDS	LHDS	HDS
Cohesive energy per atom (eV/atom)	4.877	4.663	4.483	4.471
Cohesive energy per area (eV/Å^2)	0.759	0.887	0.938	1.014

to form the peculiar fivefold coordination. However, it fails to compensate the sixfold coordination of Si atoms forming the middle atomic layer of FDS. This arguments led us to investigate another dumbbell structure that has even larger cohesive energy per atom compared to HDS. This structure has two dumbbell units arranged in a honeycomb lattice in a 2×2 unit cell. Here the packing of dumbbell units is dense compared to TDS but sparse compared to HDS. In this structure, the honeycomb lattice formed by dumbbell units is larger compared to the one formed in HDS, hence we refer to this structure as large honeycomb dumbbell silicene (LHDS). As seen in Fig. 8.4d, the maximum coordination of Si atoms in the LHDS is four. Since there are more dumbbell units in LHDS compared to TDS and no hypervalent Si atoms as in HDS, the cohesive energy per atom of freestanding LHDS is higher than both TDS and HDS.

Unlike the 3×3 silicene that matches the 4×4 Ag(111) supercell, the dumbbell structures cannot be matched because their lattice constant is squeezed as the density of dumbbell units is increased as seen in Table 8.1. To include the effect of Ag, the 4×4 Ag(111) slab composed of five layers is first squeezed to match the lattice of the 3×3 supercell of the dumbbell structures and then the system is optimized by keeping the Ag atoms fixed. Then the energy of the squeezed Ag substrate in the absence of Si atoms is calculated. The energy difference between these two systems gives the cohesive energies of the dumbbell structures. As seen in Table 8.2, the cohesive energy per Si atom is maximized in the 3×3 silicene while the cohesive energy per area is maximized for the $\sqrt{3} \times \sqrt{3}$ HDS structure. According to the model, when Si atoms are first deposited on Ag(111) substrate, they form the 3×3 reconstructed silicene that has the highest cohesive energy per Si atom, as seen in Table 8.2. At first, the dumbbell units that spontaneously form on 3×3 silicene diffuse and annihilate at the edges and contribute to the growth of even larger 3×3 regions. Once 3×3 silicene reaches sufficiently large area, the dumbbell units compete to form the most energetic structure in a given area covered by 3×3 silicene. To achieve the highest cohesive energy per area, the dumbbell units arrange themselves to form the $\sqrt{3} \times \sqrt{3}$ HDS structure.

The schematic sketch of this growth model is presented in Fig. 8.5a. This picture is in accordance with experiments in which the $\sqrt{3} \times \sqrt{3}$ structure usually appears as islands on top of the first 3×3 silicene layer. As seen in Fig. 8.5b, d, the model also excellently reproduces the distance between $\sqrt{3} \times \sqrt{3}$ and 3×3 surfaces measured

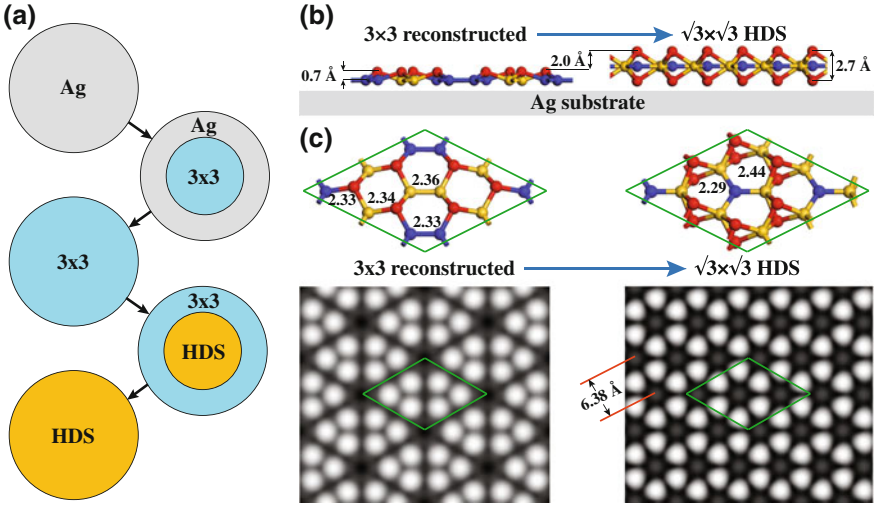

Fig. 8.5 **a** Growth sequence of the 3×3 reconstructed silicene and of the HDS structure on the Ag(111) substrate. **b** Schematic depiction of the structural transformation from the 3×3 to the $\sqrt{3} \times \sqrt{3}$ reconstruction from the side view. **c** Tilted view of the atomic structures and calculated STM images. Green lozenges represent the 3×3 supercell

to be ∼2Å [45]. Furthermore, as shown in Fig. 8.5c, e, the simulated STM image of HDS has the same honeycomb pattern as the one obtained in experiments while the $\sqrt{3} \times \sqrt{3}$ lattice constant of HDS that is calculated to be 6.38 Å, excellently matches the measured value that is ∼6.4 Å [7, 15, 45]. Also, according to the model, the $\sqrt{3} \times \sqrt{3}$ silicene forms by morphing the 3×3 and $\sqrt{7} \times \sqrt{7}$ reconstructed monolayers and this is in agreement with two experimental observation. First, in experiments, the $\sqrt{3} \times \sqrt{3}$ silicene appears after the 3×3 structure. Second, it was demonstrated that the $\sqrt{3} \times \sqrt{3}$ structures can inherit the four domains originating from the matching of the $\sqrt{7} \times \sqrt{7}$ silicene with $\sqrt{13} \times \sqrt{13}$ Ag(111) supercell [37]. Finally, this model can also be extended to explain multilayers that have $\sqrt{3} \times \sqrt{3}$ reconstruction as discussed below.

8.4 Multilayer Silicene

When Si deposition is prolonged beyond the formation of the first layer $3 \times 3/4 \times 4$ or $\sqrt{7} \times \sqrt{7}/\sqrt{13} \times \sqrt{13}$ phases and in the same conditions, growth of multi-layer silicene, which possesses a unique $\sqrt{3} \times \sqrt{3}$R(30°) (in short $\sqrt{3} \times \sqrt{3}$) structure is obtained. Such films grow in successive terraces, each showing this unique reconstruction. If growth occurs on the prototype $3 \times 3/4 \times 4$ phase, one gets a single orientation of these terraces. Instead, if growth occurs on the initial $\sqrt{7} \times \sqrt{7}/\sqrt{13} \times \sqrt{13}$ first layer silicene phase, rotated terraces are obtained; the rotation angles are directly

related to those of the first layer domains [37]. In angle-resolved photoemission (ARPES) measurements, these films possess a Dirac cone at the centre of the Brillouin zone due to back folding of the $\sqrt{3} \times \sqrt{3}$ silicene superstructure with a Fermi velocity about half that of the free standing graphene [9, 11]. Vogt et al. have studied terraces with up to five layers of $\sqrt{3} \times \sqrt{3}$ silicene. They have shown that the height difference between adjacent terraces is ∼3.1 Å [45]. Using in situ a four probe scanning tunneling microscope, a sheet resistance analogous to that of thin films of graphite in nano-grains was determined. De Padova et al. took this even further and synthesized few tens monolayers of silicene with $\sqrt{3} \times \sqrt{3}$ reconstruction. Remarkably, these multilayer silicene films survive after exposure in ambient air for a day at least, because just the very top layers are oxidized; the film underneath remains intact, as directly revealed via a graphite-like Raman signature [10]. Feng et al. have investigated bilayers of $\sqrt{3} \times \sqrt{3}$ silicene [15]. They have measured the quasi-particle interference of electrons in the first layer due to the scattering from the islands formed by the second layer grown on top [7]. A linear dispersion with high Fermi velocity was derived from these interference patterns.

Although multilayer silicene was grown in many experiments mentioned above its atomic structure has been a subject of debate. The experiments report a 5% contracted $\sqrt{3} \times \sqrt{3}$ structure that has a honeycomb appearance in STM imaging with a ∼3.1 Å distance between its layers. However, there is still no structural model that explains all these observations. Here we discuss the proposed models and point out their shortcomings.

The interlayer separation of multilayer silicene is very close but measurably different from that of Si(111). This inspired models of multilayer silicene that has bulk silicon-like interior with a modified surface structure. One such model is based on the Si(111)-Ag$\sqrt{3} \times \sqrt{3}$ system. The various surfaces obtained by the deposition of Ag on Si(111) substrate were studied intensively in the 1980s [12, 25, 29, 44]. One of the most favorable surfaces that were observed in experiments was the so called honeycomb-chain trimer (HCT) structure [44]. As seen in Fig. 8.6, the HCT model has a $\sqrt{3} \times \sqrt{3}$ honeycomb STM pattern that resembles the one observed in multilayer silicene experiments. Furthermore, the interlayer separation is close to the one obtained in experiments since the bulk region is basically Si(111). The HCT structure makes transition to the so-called inequivalent triangle (IET) structure at low temperatures. This transition could explain the spontaneous symmetry breaking observed in $\sqrt{3} \times \sqrt{3}$ silicene at low temperatures [6, 39]. Finally, it was argued that the slope of the linear portion of the S_1 band formed by the Si(111)-Ag$\sqrt{3} \times \sqrt{3}$ surface is comparable to that of the linear bands observed in $\sqrt{3} \times \sqrt{3}$ silicene experiments [7, 38, 39]. However, the HCT model does not account for the contraction of the lattice constant observed in experiments. Another model inspired by the bulk silicon structure is the tristable Si(111) bilayer grown on Ag substrate [19]. Here the flip-flop motion that is suggested to give rise to the honeycomb STM topographs is not supported by convincing arguments. Also it does not explain the lattice contraction and can not be extended to multilayers.

Here we present a possible growth model of multilayer silicene that produces structures which are in a good agreement with experiments in certain respects [3].

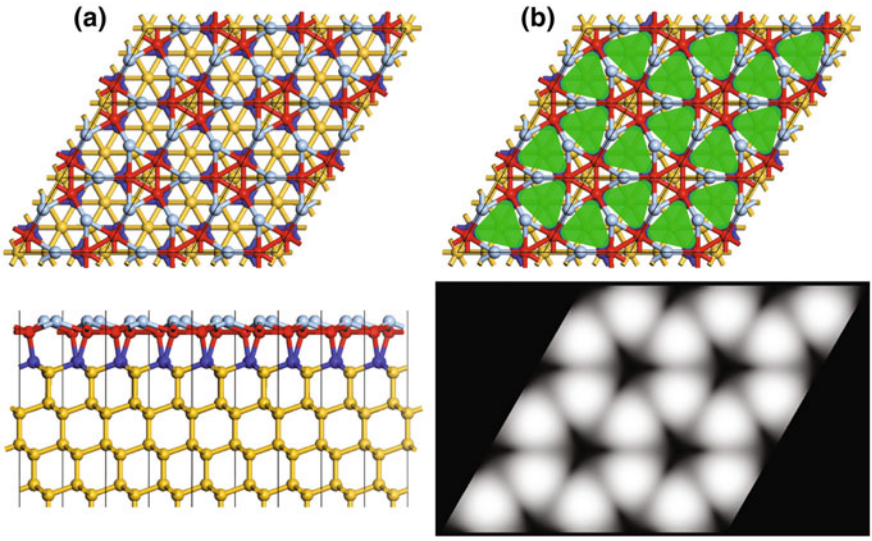

Fig. 8.6 **a** Ball and stick representation of the honeycomb-chain trimer (HCT) model [44]. The top and side views are presented in the top and bottom panels, respectively. The yellow balls are Si atoms sitting in almost ideal positions of the Si(111) substrate. The topmost layer of Si atoms and the layer below them are represented by the red and the blue balls, respectively. The Ag atoms represented by the light blue balls form the topmost atomic layer of the system by attaching to Si atoms (red balls) below them. **b** Schematic and calculated STM image of HCT structure are presented in top and bottom panels, respectively. The bright triangular spots that are observed in the STM image are represented by green triangles superimposed on the top view of the ball and stick model

This model can inspire new calculations that might eventually solve the mistery of multilayer silicene. A realistic growth simulation is really hard to do because one needs to take into account many experimental parameters. It is especially hard to run a molecular dynamics simulation long enough for the atoms to explore the whole energy landscape. Instead, we present structural relaxations accompanied with educated guesses.

A silicene monolayer is first placed on top of the already formed HDS structure, as seen in Fig. 8.7a. Upon relaxation of this system, one of the dumbbell atoms in HDS transfers to the silicene layer forming a dumbbell unit there. As a result, HDS loses one dumbbell unit and becomes TDS, while silicene sheet gains one dumbbell unit and also becomes TDS. The two TDS layers become connected to each other by covalent bonds. However, the number and strength of these vertical covalent bonds are less compared to the ones formed between two (111) planes of cubic diamond silicon (cdSi).

If we continue depositing Si atoms onto the bilayer TDS system, the TDS layer on top will first transform to HDS. This HDS layer will follow the same faith as the original HDS structure, transforming itself to TDS by donating one dumbbell to create another TDS on top, which in turn will transform to yet another HDS

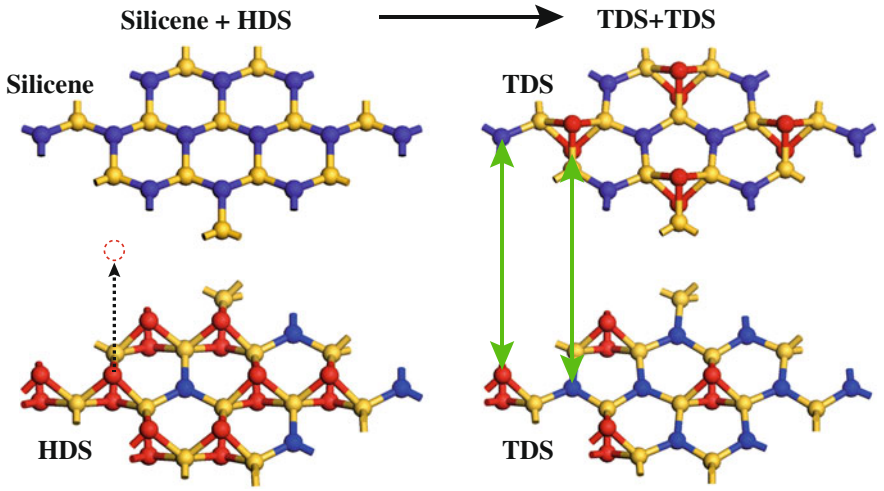

Fig. 8.7 A possible growth mechanism of multilayer silicene or silicites. When silicene is put on top of HDS, one of the dumbbell atoms transfer to the silicene layer, as shown by dashed black arrow. As a result, two TDS layers are formed, that connect to each other through covalent bonding between atoms shown by green arrows

layer. This process will continue producing multiple TDS layers connected to each other with an HDS layer on the very top. This is in agreement with experiments that continue to see the $\sqrt{3} \times \sqrt{3}$ honeycomb pattern in the STM measurements performed on multilayer silicene. It is possible to stack TDS layers in eclipsed or staggered fashion, as shown in Fig. 8.8a. The resulting bulk structures are named eclipsed (eLDS) and staggered (sLDS) layered dumbbel silicite, accordingly. All atoms in both eLDS and sLDS structure are fourfold coordinated. However, the covalent bonds significantly deviate from the ideal tetrahedral bonding angle of 109°. In the eLDS structure the TDS layers are just shifted by one third of their 2D unitcell vectors and stacked on top of each other. As shown in Fig. 8.8a, stacking follows ABCABC… and so on. It cannot be ABABAB… because in that case blue atoms would be connected to dumbbell atoms from both sides, which would unfavorably increase their coordination from four to five. The stacking of the sLDS structure is similar, but the layers are staggered with respect to each other. This is represented by a bar on top of the staggered layers.

Both eLDS and sLDS are open structures similar to the structure of cubic silicon. In fact, the mass densities of eLDS (2.10 g/cm^3) and sLDS (2.11 g/cm^3) are smaller than that of cdSi (2.28 g/cm^3). The inplane lattice constant of LDS structures is 6.47 Å which is in agreement with experiments. Note that, this is the only model that accounts for inplane lattice contraction of multilayer silicene. The interlayer distance in both eLDS and sLDS structures are around 4.3 Å. This is in contrast to experiments that find the interlayer distance to be 3.1 Å. Further work needs to be done to resolve this disagreement between theory and experiment. Due to the

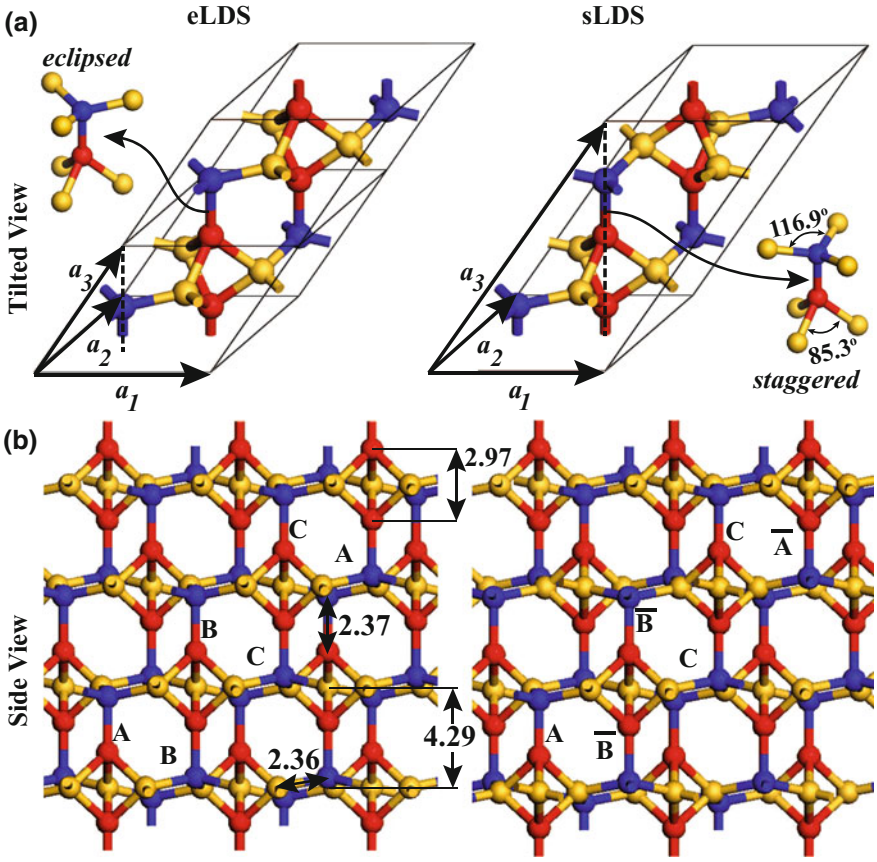

Fig. 8.8 **a** The double unit cell of eclipsed layered dumbbell silicite (eLDS) including $N = 7$ Si atoms per unit cell and single unit cell of staggered layered dumbbell silicite (sLDS) including $N = 14$ Si atoms per unit cell. **b** Side view showing the ABCABC… stacking of eLDS and the $A\bar{B}C\bar{A}B\bar{C}A$… stacking of sLDS. The bond lengths are given in Angström [3]

covalent bonds connecting LDS layers, the interlayer interaction is not like the weak van der Waals interaction found in graphite or MoS_2. However, these covalent bonds are sparse compared to those found between Si(111) layers in cubic silicon. The calculated cohesive energies are 4.42 eV and 4.43 eV per atom for eLDS and sLDS, respectively which is very close to that of cdSi (4.60 eV).

The electronic structures of eLDS and sLDS phases have indirect band gaps, which are wider than that of cdSi, as shown in Fig. 8.9a. The calculated indirect (direct) band gaps of eLDS and sLDS are 0.98 (1.43) eV and 1.26 (1.65) eV, respectively. The indirect band gap of cdSi is 0.62 eV at the DFT-PBE level while it is increased to 1.12 eV upon including many-body self-energy corrections at the G_0W_0 level [21, 40]. With G_0W_0 correction the indirect band gap of eLDS increased to 1.52 eV.

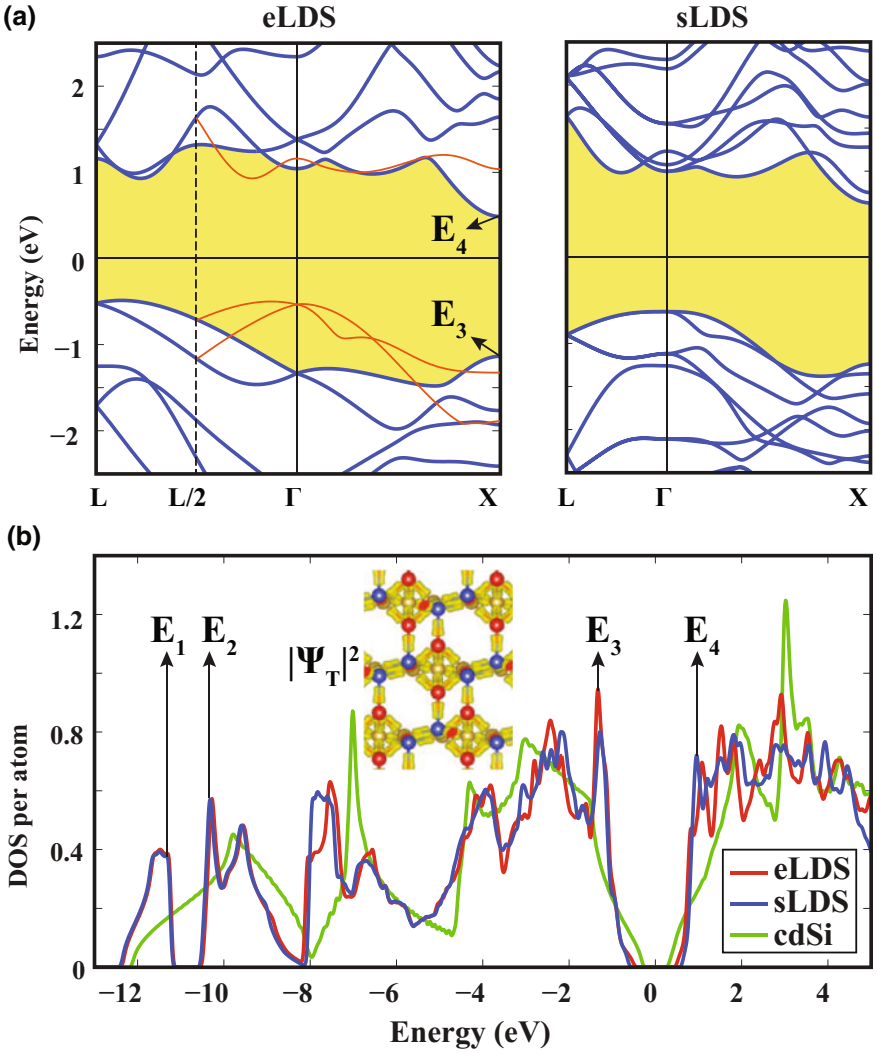

Fig. 8.9 **a** Energy band structure of eLDS and sLDS. Zero of energy is set to the the Fermi level. Bands of eLDS folded by doubling the unit cell along a_3 are shown by red lines. **b** Normalized densities of states (DOS) of eLDS, sLDS and cdSi. The isosurfaces of the total charge density shown by inset confirm the layered nature

Indirect (direct) band gaps of eLDS and sLDS calculated by HSE06 hybrid functional are 1.92 eV (2.37 eV) and 1.88 eV (2.26 eV), respectively.

Owing to the different Brillouin zones it is difficult to directly compare the band structures of LDS and cdSi. Therefore the effects of the layered character on the electronic structure are sought in the normalized densities of states (DOS). Figure 8.9b

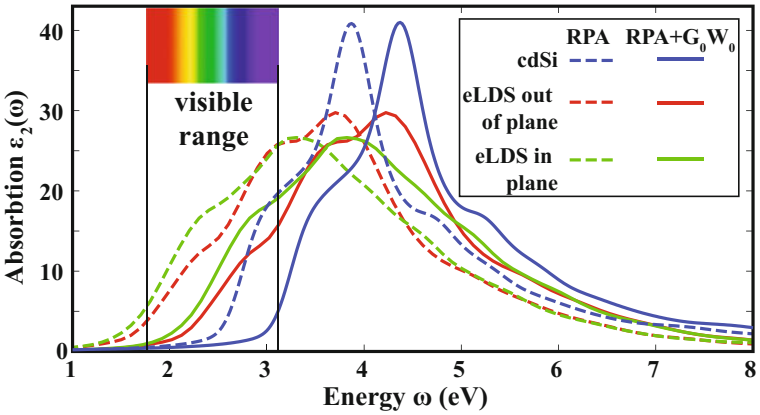

Fig. 8.10 The calculated Kohn-Sham and G_0W_0 RPA optical absorption spectra for eLDS and cdSi

shows the normalized DOSs of eLDS, sLDS and cdSi. Except for some peak shifts, the DOSs of silicites are similar. Owing to the fourfold coordination of Si atoms in all structures, the overall features of DOSs of LDS structures appear to be reminiscent of that of cdSi. This confirms the fact that the overall features of the bands of cdSi can be obtained within the first nearest neighbor coupling [20]. The total charge density, $|\Psi_T|^2$ presented by inset, depicts that electrons are mainly confined to TDS layers. This is another clear manifestation of the layered character of eLDS and sLDS phases. On the other hand, significant differences are distinguished in the details of the electronic energy structures due to deviations from tetrahedral coordination: (i) Indirect band gaps relatively larger than that of cdSi can offer promising applications in micro and nanoelectronics. (ii) Sharp peaks E_3 and E_4 near the edges of the valence and conduction bands, originate from the states, which are confined to TDS layers and can add critical functionalities in optoelectronic properties. (iii) A gap opens near the bottom of the valence band at ~ -11 eV; its edge states are also confined to TDS layers.

The in-plane and out of plane static dielectric responses also reflect the layered nature of silicite. As a matter of fact, the calculated in-plane dielectric constant of eLDS (sLDS) is $\varepsilon_{\parallel} = 12.52$ (12.85), while its out of plane dielectric constant is $\varepsilon_{\perp} = 11.69$ (11.56). Those values are contrasted with the uniform dielectric constant, $\varepsilon = 12.19$ of cdSi. In Fig. 8.10 we present the optical absorption spectra of eLDS and cdSi calculated at the RPA level using the Kohn-Sham wave functions and G_0W_0 corrected eigenvalues. The frequency dependent dielectric matrix takes different values in the in-plane and out of the plane directions of eLDS while for cdSi it is isotropic. One can see that the optical absorption of eLDS is significantly enhanced in the visible range compared to cdSi which makes it a potential candidate material for photovoltaic applications. This enhancement is still present when we rigidly shift the absorption spectra by the amount we get from G_0W_0 corrections [33].

In closing, we would like to stress that, although LDS structures fail to explain the interlayer distance or metallicity of multilayer silicene, they are novel and interesting allotropes of silicon inspired by experiments. We believe that the search for a modified version of LDS model that might fully explain the multilayer silicene experiments is worth pursuing.

References

1. G. Brumfiel, Sticky problem snares wonder material. Nature **495**, 152–153 (2013)
2. S. Cahangirov, M. Audiffred, P. Tang, A. Iacomino, W. Duan, G. Merino, A. Rubio, Electronic structure of silicene on Ag(111): strong hybridization effects. Phys. Rev. B **88**, 035432 (2013)
3. S. Cahangirov, V.O. Özçelik, A. Rubio, S. Ciraci, Silicite: the layered allotrope of silicon. Phys. Rev. B **90**, 085426 (2014a)
4. S. Cahangirov, V.O. Özçelik, L. Xian, J. Avila, S. Cho, M.C. Asensio, S. Ciraci, A. Rubio, Atomic structure of the $\sqrt{3} \times \sqrt{3}$ phase of silicene on Ag(111). Phys. Rev. B **90**, 035448 (2014b)
5. L. Chen, B. Feng, K. Wu, Observation of a possible superconducting gap in silicene on Ag(111) surface. Appl. Phys. Lett. **102**, 081602 (2013a)
6. L. Chen, H. Li, B. Feng, Z. Ding, J. Qiu, P. Cheng, K. Wu, S. Meng, Spontaneous symmetry breaking and dynamic phase transition in monolayer silicene. Phys. Rev. Lett. **110**, 085504 (2013b)
7. L. Chen, C.C. Liu, B. Feng, X. He, P. Cheng, Z. Ding, S. Meng, Y. Yao, K. Wu, Evidence for Dirac fermions in a honeycomb lattice based on silicon. Phys. Rev. Lett. **109**, 056804 (2012)
8. M.X. Chen, M. Weinert, Revealing the substrate origin of the linear dispersion of silicene/Ag(111). Nano Lett. (2014)
9. P. De Padova, J. Avila, A. Resta, I. Razado-Colambo, C. Quaresima, C. Ottaviani, B. Olivieri, T. Bruhn, P. Vogt, M.C. Asensio, G.L. Lay, The quasiparticle band dispersion in epitaxial multilayer silicene. J. Phys.: Condens. Matter **25**, 382202 (2013)
10. P. De Padova, C. Ottaviani, C. Quaresima, B. Olivieri, P. Imperatori, E. Salomon, T. Angot, L. Quagliano, C. Romano, A. Vona, M. Muniz-Miranda, A. Generosi, B. Paci, G.L. Lay, 24 h stability of thick multilayer silicene in air. 2D Mater. **1**, 021003 (2014)
11. P. De Padova, P. Vogt, A. Resta, J. Avila, I. Razado-Colambo, C. Quaresima, C. Ottaviani, B. Olivieri, T. Bruhn, T. Hirahara, T. Shirai, S. Hasegawa, M. Carmen Asensio, G. Le Lay, Evidence of Dirac fermions in multilayer silicene. Appl. Phys. Lett. **102**, 163106 (2013)
12. Y.G. Ding, C.T. Chan, K.M. Ho, Structure of the $(\sqrt{3} \times \sqrt{3})$R30° Ag/Si(111) surface from first-principles calculations. Phys. Rev. Lett. **67**, 1454–1457 (1991)
13. S. Dutta, K. Wakabayashi, Momentum shift of Dirac cones in the silicene-intercalated compound $CaSi_2$. Phys. Rev. B **91**, 201410 (2015)
14. M. Ezawa, Valley-polarized metals and quantum anomalous Hall effect in silicene. Phys. Rev. Lett. **109**, 055502 (2012)
15. B. Feng, Z. Ding, S. Meng, Y. Yao, X. He, P. Cheng, L. Chen, K. Wu, Evidence of silicene in honeycomb structures of silicon on Ag(111). Nano Lett. **12**, 3507–3511 (2012)
16. A. Fleurence, R. Friedlein, T. Ozaki, H. Kawai, Y. Wang, Y. Yamada-Takamura, Experimental evidence for epitaxial silicene on diboride thin films. Phys. Rev. Lett. **108**, 245501 (2012)
17. Y. Fukaya, I. Mochizuki, M. Maekawa, K. Wada, T. Hyodo, I. Matsuda, A. Kawasuso, Structure of silicene on a Ag(111) surface studied by reflection high-energy positron diffraction. Phys. Rev. B **88**, 205413 (2013)
18. Z.X. Guo, S. Furuya, J.I. Iwata, A. Oshiyama, Absence and presence of Dirac electrons in silicene on substrates. Phys. Rev. B **87**, 235435 (2013)

19. Z.X. Guo, A. Oshiyama, Structural tristability and deep Dirac states in bilayer silicene on Ag(111) surfaces. Phys. Rev. B **89**, 155418 (2014)
20. W.A. Harrison, S. Ciraci, Bond-orbital model II. Phys. Rev. B **10**, 1516–1527 (1974)
21. L. Hedin, New method for calculating the one-particle Green's function with application to the electron-gas problem. Phys. Rev. **139**, A796–A823 (1965)
22. D. Kaltsas, L. Tsetseris, Stability and electronic properties of ultrathin films of silicon and germanium. Phys. Chem. Chem. Phys. **15**, 9710–9715 (2013)
23. K. Kawahara, T. Shirasawa, R. Arafune, C.L. Lin, T. Takahashi, M. Kawai, N. Takagi, Determination of atomic positions in silicene on Ag(111) by low-energy electron diffraction. Surface Sci. **623**, 25–28 (2014)
24. G. Le Lay, Physics and electronics of the noble-metal/elemental-semiconductor interface formation: a status report. Surface Sci. **132**, 169–204 (1983)
25. G. Lelay, M. Manneville, R. Kern, Cohesive energy of the two-dimensional Si(111) 3×1 Ag and Si(111)$\sqrt{3}$-R(30°) Ag phases of the silver (deposit)-silicon(111) (substrate) system. Surface Sci. **72**, 405–422 (1978)
26. C.L. Lin, R. Arafune, K. Kawahara, M. Kanno, N. Tsukahara, E. Minamitani, Y. Kim, M. Kawai, N. Takagi, Substrate-induced symmetry breaking in silicene. Phys. Rev. Lett. **110**, 076801 (2013)
27. C.L. Lin, R. Arafune, K. Kawahara, N. Tsukahara, E. Minamitani, Y. Kim, N. Takagi, M. Kawai, Structure of silicene grown on Ag(111). Appl. Phys. Exp. **5**, 045802 (2012)
28. C.C. Liu, W. Feng, Y. Yao, Quantum spin Hall effect in silicene and two-dimensional germanium. Phys. Rev. Lett. **107**, 076802 (2011)
29. E.J. van Loenen, J.E. Demuth, R.M. Tromp, R.J. Hamers, Local electron states and surface geometry of Si(111)-$\sqrt{3} \times \sqrt{3}$ Ag. Phys. Rev. Lett. **58**, 373–376 (1987)
30. L. Matthes, O. Pulci, F. Bechstedt, Massive Dirac quasiparticles in the optical absorbance of graphene, silicene, germanene, and tinene. J. Phys.: Condens. Matter **25**, 395305 (2013)
31. L. Meng, Y. Wang, L. Zhang, S. Du, R. Wu, L. Li, Y. Zhang, G. Li, H. Zhou, W.A. Hofer, H.J. Gao, Buckled silicene formation on Ir(111). Nano Lett. **13**, 685–690 (2013)
32. E. Noguchi, K. Sugawara, R. Yaokawa, T. Hitosugi, H. Nakano, T. Takahashi, Direct observation of Dirac cone in multilayer silicene intercalation compound $CaSi_2$. Adv. Mater. **27**, 856–860 (2015)
33. G. Onida, L. Reining, A. Rubio, Electronic excitations: density-functional versus many-body Green's-function approaches. Rev. Mod. Phys. **74**, 601–659 (2002)
34. V.O. Özçelik, S. Ciraci, Local reconstructions of silicene induced by adatoms. J. Phys. Chem. C **117**, 26305–26315 (2013)
35. V.O. Özçelik, H.H. Gurel, S. Ciraci, Self-healing of vacancy defects in single-layer graphene and silicene. Phys. Rev. B **88**, 045440 (2013)
36. A. Resta, T. Leoni, C. Barth, A. Ranguis, C. Becker, T. Bruhn, P. Vogt, G.L. Lay, Atomic structures of silicene layers grown on Ag(111): scanning tunneling microscopy and noncontact atomic force microscopy observations. Sci. Rep. **3** (2013)
37. E. Salomon, R.E. Ajjouri, G.L. Lay, T. Angot, Growth and structural properties of silicene at multilayer coverage. J. Phys.: Condens. Matter **26**, 185003 (2014)
38. N. Sato, T. Nagao, S. Hasegawa, Si(111)-($\sqrt{3} \times \sqrt{3}$)-Ag surface at low temperatures: symmetry breaking and surface twin boundaries. Surface Sci. **442**, 65–73 (1999)
39. T. Shirai, T. Shirasawa, T. Hirahara, N. Fukui, T. Takahashi, S. Hasegawa, Structure determination of multilayer silicene grown on Ag(111) films by electron diffraction: evidence for Ag segregation at the surface. Phys. Rev. B **89**, 241403 (2014)
40. M. Shishkin, G. Kresse, Self-consistent GW calculations for semiconductors and insulators. Phys. Rev. B **75**, 235102 (2007)
41. R. Stephan, M.C. Hanf, P. Sonnet, Spatial analysis of interactions at the silicene/Ag interface: first principles study. J. Phys.: Condens. Matter **27**, 015002 (2015)
42. L. Tao, E. Cinquanta, D. Chiappe, C. Grazianetti, M. Fanciulli, M. Dubey, A. Molle, D. Akinwande, Silicene field-effect transistors operating at room temperature. Nat. Nanotechnol. **10**, 227–231 (2015)

43. D. Tsoutsou, E. Xenogiannopoulou, E. Golias, P. Tsipas, A. Dimoulas, Evidence for hybrid surface metallic band in (4 × 4) silicene on Ag(111). Appl. Phys. Lett. **103**, 231604 (2013)
44. E. Vlieg, A.V.D. Gon, J.V.D. Veen, J. MacDonald, C. Norris, The structure of Si(111)-($\sqrt{3} \times \sqrt{3}$)r 30°-Ag determined by surface X-ray diffraction. Surface Sci. **209**, 100–114 (1989)
45. P. Vogt, P. Capiod, M. Berthe, A. Resta, P. De Padova, T. Bruhn, G. Le Lay, B. Grandidier, Synthesis and electrical conductivity of multilayer silicene. Appl. Phys. Lett. **104**, 021602 (2014)
46. P. Vogt, P. De Padova, C. Quaresima, J. Avila, E. Frantzeskakis, M.C. Asensio, A. Resta, B. Ealet, G. Le Lay, Silicene: compelling experimental evidence for graphenelike two-dimensional silicon. Phys. Rev. Lett. **108**, 155501 (2012)
47. Y.P. Wang, H.P. Cheng, Absence of a Dirac cone in silicene on Ag(111): first-principles density functional calculations with a modified effective band structure technique. Phys. Rev. B **87**, 245430 (2013)
48. Y. Xu, B. Yan, H.J. Zhang, J. Wang, G. Xu, P. Tang, W. Duan, S.C. Zhang, Large-gap quantum spin Hall insulators in tin films. Phys. Rev. Lett. **111**, 136804 (2013)
49. X.S. Ye, Z.G. Shao, H. Zhao, L. Yang, C.L. Wang, Intrinsic carrier mobility of germanene is larger than graphene's: first-principle calculations. RSC Adv. **4**, 21216–21220 (2014)
50. L.D. Zhang, F. Yang, Y. Yao, Possible electric-field-induced superconducting states in doped silicene. Sci. Rep. **5** (2015)